ISSN: 2710-0588

Numerical Analysis of Mechanical Properties of White Sandstone Granite Composite Rock Mass with Prefabricated Cracks

Ti Su

School of Civil Engineering, Henan Polytechnic University, Jiaozuo 454003, Henan, China

Abstract

The development and propagation of fractures within rocks have a significant impact on their mechanical behavior and engineering stability. This study focuses on composite rock masses composed of sandstone and granite and uses the PFC2D numerical simulation platform based on the discrete element method to systematically investigate the mechanical responses, damage evolution, and failure patterns of composite rock masses containing pre-existing fractures under uniaxial compression. By constructing models of pre-existing fractures with different inclinations 0°, 15°, 30°, 45°, 60°, 75° and lengths 10 mm, 15 mm, 20 mm, 25 mm, the influence of fracture geometric parameters on peak strength, peak strain, elastic modulus, and crack propagation paths of the rock masses was analyzed. The results indicate that when the fracture inclination is 30°, both the peak strength and peak strain of the rock mass are lowest, showing the most significant degradation effect; when the inclination is 75°, the mechanical performance of the rock mass is optimal. The influence of fracture length is regulated by the inclination: at 30°, the elastic modulus decreases with increasing fracture length, while at 60°, the effect is not significant. The crack initiation location and final failure mode exhibit regular evolution with changing inclination, with 45° being the optimal angle for shear-through failure.

Keywords

Mixed rock mass; Prefabricated cracks; Mechanical properties; Damage evolution; destruction mode.

1. Introduction

As a natural civil engineering material widely used in mines, tunnels, underground spaces and other engineering projects, the deformation and failure mechanism of rock are directly related to the engineering safety issues such as slope stability and surrounding rock control of caverns. In the natural state, rocks often contain fractures of different scales. Under the action of external stress, these fractures are prone to stress concentration at their ends, which promotes the further propagation of fractures and thus significantly reduces the overall strength of rocks. A large number of studies have shown that the bearing capacity of fractured rock is much lower than that of intact rock, so fractures are regarded as a key factor controlling the mechanical behavior of rock. Against this background, the systematic study on the mechanical properties and crack propagation laws of rock with prefabricated cracks has important theoretical value and engineering guiding significance for deeply revealing the rock mass failure mechanism and improving the design of related projects and disaster prevention and control capabilities. Foreign scholar Ohnaka [1] carried out a special study on the uniaxial loading condition of rock, focusing on analyzing the evolution characteristics of rock acoustic emission frequency and the propagation law of internal fractures during the loading process. In rock mechanical tests with fractures and cavity defects, natural rock defects are random and uncontrollable, and when prefabricating defects in artificially prepared rock-like materials, there are problems such as difficult control of processing accuracy, long preparation cycle and high cost, which affect the

ISSN: 2710-0588

reliability and repeatability of the tests. Therefore, numerical simulation has become a commonly used method to explore the influence of defects on rock mechanical response due to its advantages of adjustable defect parameters, controllable conditions, high efficiency and low cost. Among them, the PFC software based on the discrete element theory can effectively characterize the interaction of rock mesoscopic particles and accurately simulate the entire process of crack initiation-propagation-penetration to macroscopic failure, which is widely used in the study of rock defect mechanics [2]. Yu Qiaojun [3] carried out uniaxial compression and acoustic emission (AE) monitoring experiments on granite samples of different laboratory sizes, and established a numerical model with primary fracture network based on the PFC platform combined with XRD mineral composition constraints and AE data guidance. Wang Linfeng et al. [4] conducted uniaxial compression tests on fractured limestone samples with different dip angles, studied the macroscopic mechanical failure characteristics of fractured limestone, constructed the corresponding numerical calculation model through the particle flow platform, and revealed the mesoscopic crack propagation laws of fractured limestone with different dip angles. Yi Ting [5] under different fracture dip angles and numbers, and carried out conventional uniaxial compression tests on rock-like material specimens with different prefabricated fractures. Liu Wang [6] studied the mechanical behavior, energy dissipation characteristics and acoustic emission signal characteristics of rock with intersecting fractures during the loading process, and obtained mechanical parameters and acoustic emission characteristics by using uniaxial loading tests and acoustic emission monitoring technology. Wang Xiaoran [7][8] studied the acoustic emission response of crack propagation in fractured rock and carried out quantitative inversion of the microscopic mechanism by acoustic emission. Fakhimi et al. [9] adopted a research method combining numerical simulation and indoor physical tests to study the mechanical behavior of sandstone with holes under biaxial compression conditions, focusing on analyzing the failure mode of sandstone and the accompanying acoustic emission characteristics under this loading condition. Yin [10] constructed an analysis model with the help of discrete element numerical simulation software, carried out the simulation of uniaxial compression tests on rock samples, and systematically explored the evolution law of uniaxial compressive strength of isotropic rock when the dip angle of rock joints changes. Huang et al. [11] established a rock numerical model with specific characteristics through the numerical simulation software PFC, carried out the simulation of uniaxial compression tests on it, and compared and analyzed the mechanical performance parameters obtained from the simulation with the indoor test results, and the results showed a high consistency between the two. N. Cho [12] carried out analytical research by using the clumped particle model of rock. Wang Yunfei et al. [13][14]took granite as the research carrier, and on the basis of analyzing its strength parameters and rock burst risk characteristics, realized the visual reproduction of the internal damage evolution process of granite by obtaining the acoustic emission signal curve during the failure process. Liu Weitao [15] explored the influence of edge fractures of different lengths on the mechanical properties and crack propagation laws of rock mass through indoor tests and numerical simulation. Liu Taoying [16] constructed a two-dimensional uniaxial compression test model by using particle flow software, and analyzed the influence of fracture dip angle on rock compressive strength and crack propagation characteristics. Zhou Xiang [17] adopted indoor uniaxial compression tests combined with XTDIC and acoustic emission monitoring systems to explore the influence of fracture position, fracture dip angle and rock stratum combination mode on the mechanical behavior and failure mode of single-fracture layered composite rock samples. Fan Xiang [18] established a numerical calculation model by using the parallel bonding method in particle flow software, and studied the contact force, microfracture number and failure behavior of jointed rock mass in jointed specimens under uniaxial compression load from both mesoscopic and macroscopic aspects. Tang Zhiqiang [19] carried out biaxial compression tests on sandstone

ISSN: 2710-0588

with prefabricated cracks after corrosion based on the particle flow discrete element method, and used the particle flow PFC2D to simulate and analyze the crack initiation, propagation and penetration failure laws of fractured rock after different chemical corrosion. Zhu Dong [20] cut out arc-shaped fracture defects with different γ values in intact plate-shaped yellow sandstone samples by using a high-pressure water jet cutting machine, and adopted the YNS-2000 electro-hydraulic servo control test system, DS2 acoustic emission and digital photography acquisition system to study the influence laws of different arc-shaped fracture γ on the peak strength, average modulus, secant modulus, acoustic emission, failure process, initiation form, initiation stress and failure form of yellow sandstone under uniaxial compression.

Overall, the existing studies mostly focus on single lithology or regular prefabricated crack models, and the research on composite rock mass with prefabricated fractures composed of rocks with different mechanical properties is insufficient. As common engineering rock masses, the fracture propagation laws and overall mechanical response of white sandstone and granite under combined conditions need to be further revealed. Therefore, based on the PFC2D numerical simulation platform, this study focuses on investigating the influence of prefabricated fractures with different dip angles and lengths on the mechanical properties of white sandstone-granite composite rock mass, systematically analyzes the effects of fracture dip angle and length on the mechanical properties, mesoscopic damage evolution process and final failure mode of the samples, in order to provide a theoretical reference for the stability evaluation and disaster prevention and control of rock-like engineering.

2. Basic Theory and Sample Model

2.1. Basic Theory of Particle Flow Model

This study adopted the two-dimensional particle flow code (PFC2D) based on the discrete element method for numerical simulation. The core theory of the software is based on discontinuous medium mechanics, which regards the research object (such as rock mass) as an aggregate composed of a large number of rigid particles. PFC2D reproduces the macroscopic mechanical behavior of complex media by simulating the movement and interaction (including contact, sliding, separation and bonding) between particles.

In the numerical framework of PFC2D, the macroscopic mechanical properties of the medium are not given in advance, but are jointly determined by the geometric characteristics (such as particle size distribution) of particle units and their mesoscopic mechanical parameters (such as stiffness, friction coefficient, bonding strength). During the calculation process, the program allows small controllable overlap between particles to characterize the contact force, and strictly follows Newton's second law for cyclic calculation of force-displacement and mechanical evolution. In this study, the parallel bonding model was selected to carry out numerical simulation analysis on the entire failure evolution process of rock under uniaxial compression. This model can establish a bonding effect that can transmit both force and moment between contacting particle pairs, and its failure forms include tensile fracture and shear fracture, thus being able to naturally simulate the entire process of initiation, propagation and penetration of microcracks into macroscopic fractures in rock mass. Figure 1 is a structural schematic diagram of the parallel bonding model. Compared with the linear contact model, the parallel bonding model can more accurately reflect the real mechanical response characteristics of rock materials.

The characteristic of evolving macroscopic response from mesoscopic mechanism makes PFC2D particularly suitable for simulating the deformation and failure problems of discontinuous and inhomogeneous media such as rock materials with prefabricated fractures. By accurately calibrating the mesoscopic parameters corresponding to white sandstone and granite, the model can effectively reveal the mechanical mechanism of cracks initiating from

ISSN: 2710-0588

the tips of prefabricated fractures, interacting with the material interface and eventually losing stability in the composite rock mass.

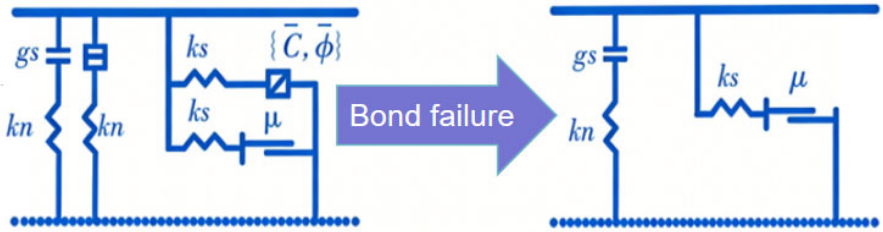

Figure 1. Parallel Bonding Model

2.2. Numerical Model and Parameter Selection

In the process of carrying out numerical simulation research on white sandstone-granite mixed rock samples by using the PFC2D discrete element software, it is necessary to accurately input two types of core parameters of the particle system and bonding units, namely geometric shape parameters and mesoscopic mechanical property parameters. The determination of the values of the above parameters is often difficult to obtain directly through theoretical derivation, and the parameter calibration is usually completed by the trial-and-error optimization method [21][22][23]-[24]. The specific operation logic of this method is to take the stress-strain curves measured in the indoor mechanical tests of single rock samples of white sandstone and granite as the calibration benchmark, adjust key mesoscopic parameters such as particle radius and bonding stiffness cyclically, perform numerical simulation calculations for many times, compare and analyze the morphological characteristics of the stress-strain curves output by the simulation and the indoor test curves, until the key indicators such as the slope of the rising section, peak strength and post-peak attenuation trend of the two achieve a high degree of matching, so as to determine the optimal combination of mesoscopic parameters suitable for the simulation of mixed rock samples.

Table 1. Micro mechanical parameters

Micro mechanical parameters	Sandstone	Granite
Maximum particle size/mm	0.4	0.4
Minimum particle size/mm	0.2	0.2
Particle density kg/m^3	2800	2800
Particle size ratio Dmax/Dmin	2	2
Particle to particle contact	Contact models: parallel bond models	
Particle contact modulus/Gpa	1	1
Particle contact stiffness kn/ks	1.33	1.33
Tensile strength MPa	39	102
Bond strength MPa	150	393
Friction coefficient	0.65	0.75
Internal friction angle	30°	30°
Contact between particles and wall	Contact model: linear bond model	
Particle contact modulus/Gpa	30	30
Particle contact stiffness kn/ks	2.4	2.4
Friction coefficient	0.3	0.3

After parameter debugging, the finally determined mesoscopic mechanical parameters of particles and bonding are listed in Table 1. It can be seen from the curve comparison results in Figure 2(a) and Figure 2(b) that the deviation of the numerical simulation curves from the test

ISSN: 2710-0588

curves of white sandstone and granite samples is small in the two key mechanical indicators of peak strength and peak strain, which indicates that the setting of various mesoscopic parameters in the current PFC simulation is reasonable and can meet the accuracy requirements of the subsequent simulation analysis of mixed samples.

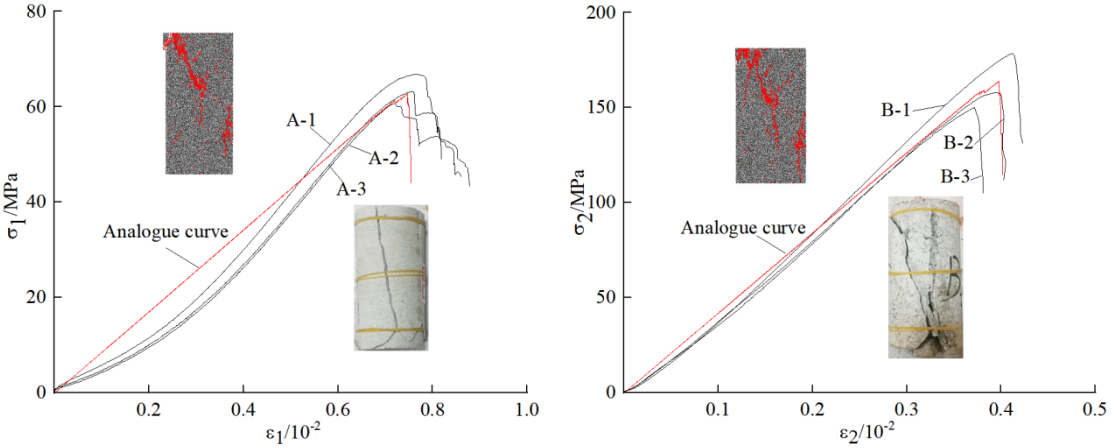

(a)Sandstone stress-strain curve (b)Granite stress-strain curve

Figure 2. Laboratory experiment

2.3. Numerical Simulation Scheme

In the numerical simulation of this study, the geometric size of the constructed model was set to 50 mm (horizontal) × 100 mm (vertical). The design of prefabricated fractures in the simulation scheme included two key variables: one was the fracture dip angle α, with 6 gradient levels set at 0°, 15°, 30°, 45°, 60° and 75° respectively; the other was the fracture length d, covering 4 different values of 10 mm, 15 mm, 20 mm and 25 mm in turn.

3. Analysis of Simulation Results

3.1. Influence of Different Fracture Dip Angles on Mechanical Properties

Numerical simulation of uniaxial compression tests on a series of rock samples with different prefabricated crack dip angles was carried out by using PFC2D software. The loading termination condition of the test was set that the stress reached 70% of the peak stress of the sample, and the stress-strain relationships of the models with different dip angles obtained are shown in Figure 3.

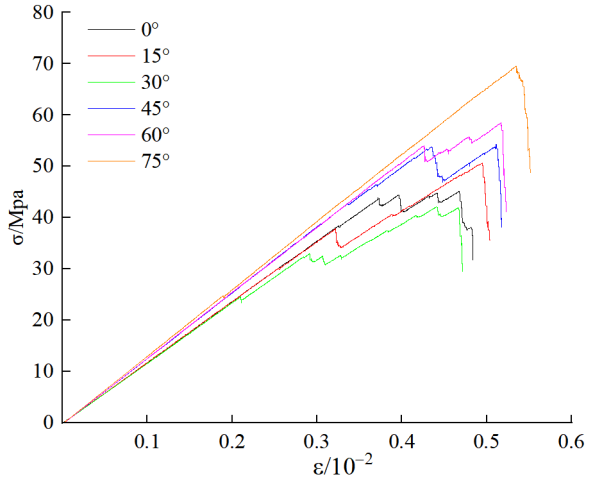

Figure 3. Stress-strain curves at different angles

ISSN: 2710-0588

In the initial stage of loading, the curves of all fracture dip angles rise approximately linearly, indicating that the rock mass is in the elastic deformation stage. In this stage, there is no obvious propagation of microcracks inside the rock mass, and the stress is proportional to the strain, which conforms to Hooke's law. There are differences in the slope of the elastic stage for different fracture dip angles: the curve slope of the fracture dip angle of 75° is the largest, with the fastest stress growth rate; the curve slope of 30° is relatively the smallest, with relatively gentle stress growth.

When the strain exceeds a certain threshold, the curve deviates from linearity and enters the yield and failure stage, and the rock mass with different fracture dip angles shows obvious differences in failure modes.

When the fracture dip angle is 30°, the peak stress and peak strain are the smallest. In addition, with the continuous increase of the fracture dip angle, both the peak stress and peak strain increase continuously. Moreover, when the fracture dip angle reaches 75°, the fracture has a great influence on the peak stress and peak strain, far exceeding the influence of other fracture dip angles.

The rock mass with a fracture dip angle of 75° has the highest stress peak, indicating that under the test conditions, the fracture with this dip angle has the weakest weakening effect on the rock mass strength; while the rock mass with a fracture dip angle of about 30° has a lower stress peak, reflecting that the fracture with this dip angle has a more significant degradation effect on the rock mass strength. This law is closely related to the stress mechanism of the fracture surface: under axial load, fractures with different dip angles have different distribution ratios of normal stress and shear stress, which in turn leads to differences in the failure initiation position, propagation path and final strength of the rock mass.

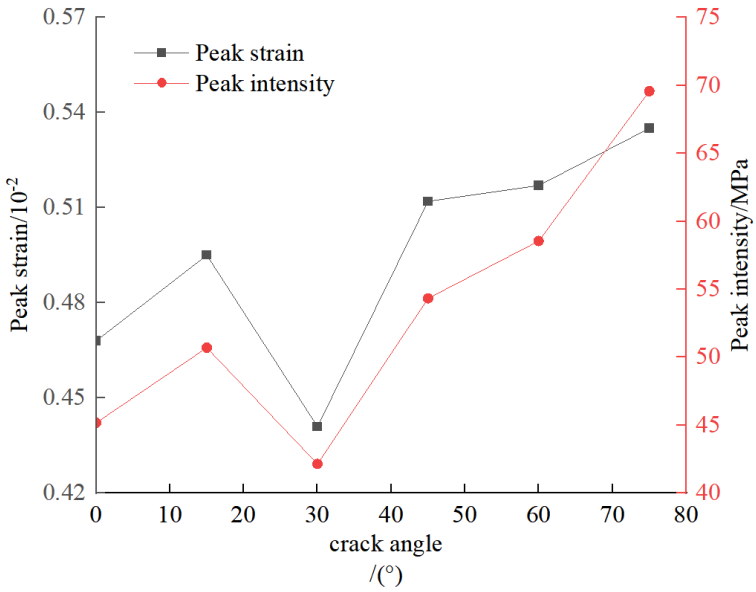

Figure 4. Peak strain peak intensity curves at different inclination angles

It can be seen from the figure that in the range of 0°-30°, both curves show a trend of first rising and then falling. The peak strain reaches a local peak at about 15°, and the peak strength also reaches a local peak at about 15°; then both decrease synchronously and drop to the minimum at 30°. In the range of 30°-75°, both curves show a continuous rising trend, and it can be seen from the slope that the rising rate is gradually accelerated, and finally both reach the maximum at 75°.

ISSN: 2710-0588

When the fracture dip angle is 30°, both the peak strain and peak strength reach the minimum value simultaneously. From the perspective of rock mass mechanics, the angle between the fracture surface and the loading direction at this time makes the rock mass more prone to slip failure along the fracture surface, resulting in a significant reduction in both the peak strength and peak strain of the rock mass. When the fracture dip angle is 75°, both the peak strain and peak strength reach the maximum value simultaneously. At this time, the angle between the fracture surface and the loading direction inhibits the slip effect of the fracture surface, and the rock mass is closer to the stress state of the intact rock mass, so the bearing capacity and deformation capacity both reach the optimal level.

3.2. Influence of Different Fracture Lengths on Mechanical Properties

To clarify the influence of the change of prefabricated crack length on rock mechanical characteristics, this study adopted the uniaxial compression numerical simulation method to carry out relevant simulation tests on rock models with prefabricated crack dip angles of 30° and 60° and crack lengths of 10 mm, 15 mm, 20 mm and 25 mm in turn, and then obtained the corresponding stress-strain curves, as shown in Figure 5 in detail.

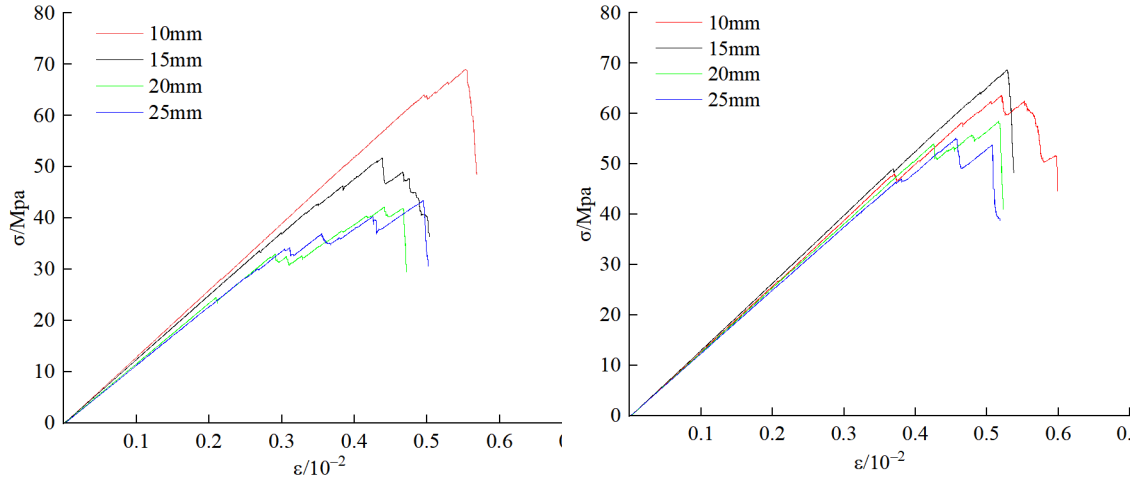

Figure 5. Stress strain curves with different crack lengths

It can be observed from the figure that when the fracture dip angle is 30°, in the range of fracture length from 10 mm to 20 mm, the peak stress and peak strain show a downward trend with the increase of fracture length; while when the fracture length reaches 25 mm, the peak stress and peak strain show a slight rebound. For the case of a fracture dip angle of 60°, in the range of fracture length from 10 mm to 15 mm, the peak stress increases with the increase of fracture length, and then in the range of 15 mm to 25 mm, the peak stress gradually decreases with the increase of fracture length, while the peak strain remains at a relatively close level. To more intuitively analyze the action law of fracture length on peak stress and peak strain, fitting processing was carried out on fracture length, peak stress and peak strain, and the fitting results are shown in Figure 6.

ISSN: 2710-0588

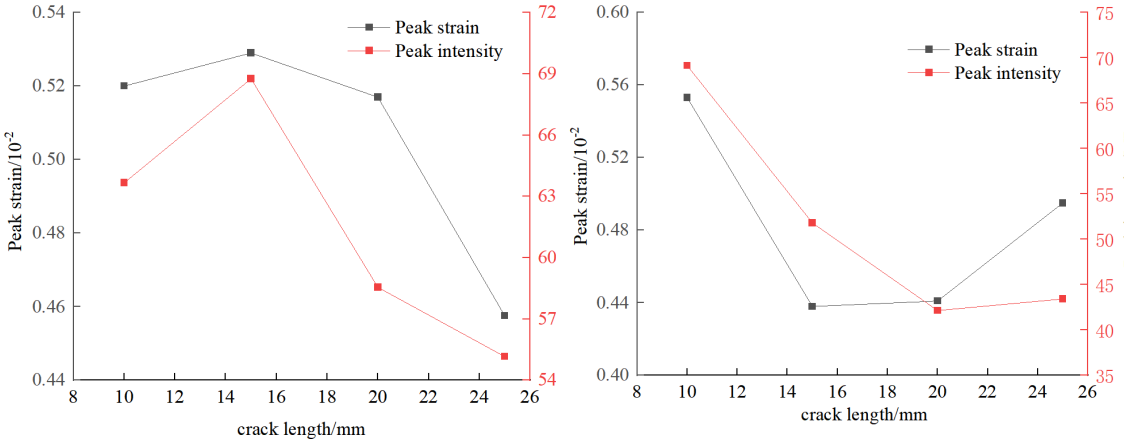

Figure 6. Peak strain peak strength curves with different crack lengths

It can be seen from the figure 7 that at a dip angle of 30°, both the peak strength and peak strain of the model show a trend of first decreasing and then increasing. The peak strain shows a downward trend with a fast decline rate in the range of fracture length from 10 mm to 15 mm, and an upward trend with a slow rise rate in the range of fracture length from 15 mm to 25 mm; the peak strength shows a downward trend with a decline rate of first slow and then fast in the range of fracture length from 10 mm to 20 mm, and an upward trend with a slow rise rate in the range of fracture length from 20 mm to 25 mm. At a dip angle of 60°, both the peak strength and peak strain of the model show a trend of first rising and then falling. The peak strain rises slowly in the range of fracture length from 10 mm to 15 mm, and the decline rate is first slow and then fast in the range of 15 mm to 25 mm; the peak strength rises rapidly in the range of fracture length from 10 mm to 15 mm, and drops rapidly in the range of 15 mm to 25 mm. In summary, when the crack length changes, the degree of influence of the dip angle on the peak stress and peak strain is different.

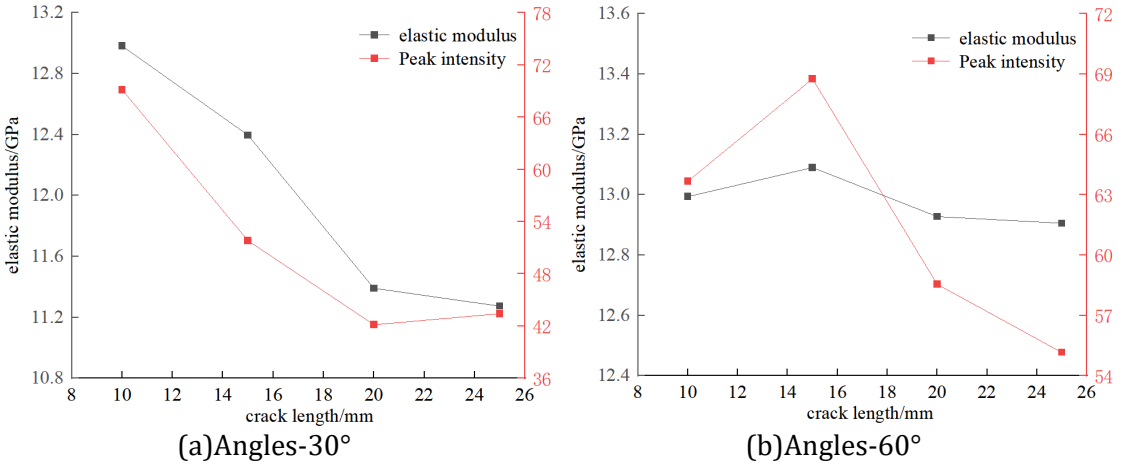

Figure 7. Elastic modulus and peak strength curves with different crack lengths

As shown in the figure, the elastic modulus has a similar trend with the peak strength. When the fracture dip angle is 30°, the elastic modulus shows a downward trend with the increase of fracture length; while when the fracture dip angle is 60°, the elastic modulus has no significant fluctuation. It can be inferred that in the case of a relatively small fracture dip angle, the elastic

ISSN: 2710-0588

modulus of the sample decreases gradually with the increase of fracture length. When the fracture dip angle increases to a specific value, the fracture length no longer has an obvious effect on the elastic modulus of the sample.

4. Crack Propagation and Evolution

4.1. Crack Initiation Location

The initiation locations of fractures with different dip angles during uniaxial compression in the tests are shown in Figure 8. It can be seen from Figure 8 that when the dip angle of the prefabricated fracture is 0°, the crack initiation location is not at the tip of the prefabricated fracture, but around the prefabricated fracture. For the samples with prefabricated fracture dip angles of 15°-45°, the initiation location starts at the tip of the prefabricated fracture. With the continuous increase of the dip angle of the prefabricated fracture, when the dip angle reaches 60°-75°, the crack initiation location returns to the vicinity of the prefabricated fracture and no longer occurs at the tip of the prefabricated fracture. Although the stress concentration degree at its location is not as high as that at the tip of the prefabricated fracture, it reaches the initiation condition first due to its extremely low strength and becomes the crack initiation source. It can also be observed that except when the dip angle of the prefabricated fracture is 45°, the crack initiation locations all occur on the side of the sandstone sample with lower strength, and it is difficult to cause damage on the side of the granite sample. In summary, prefabricated fractures with different dip angles have a significant impact on the initiation location of the sample.

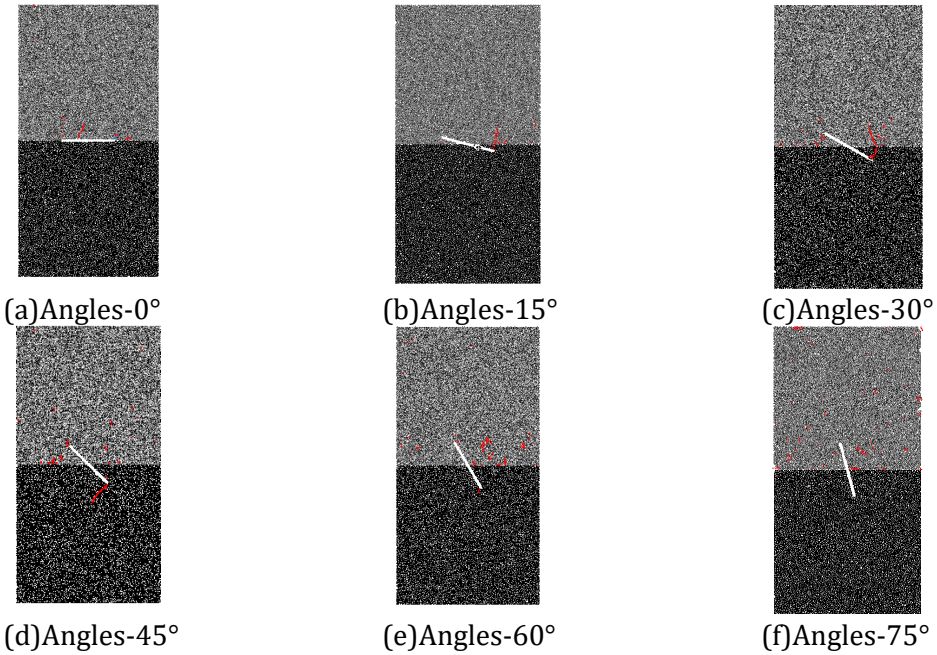

Figure 8. Crack initiation location

4.2. Mesoscopic Damage Evolution Process

The mesoscopic damage evolution processes of samples with different crack dip angles during loading are shown in Table 2. Three characteristic points (I, II, III) in the compression process were analyzed, where I represents the initiation location, II represents the stable propagation stage, and III represents the peak stress. The force chain evolution and crack classification at different characteristic points were discussed. In the force chain diagram, blue represents the compressed part and green represents the tensioned part, while in the crack classification diagram, red represents tensile cracks and black represents shear cracks.

ISSN: 2710-0588

Table 2. Microscopic damage evolution process

Angles	Type	I	II	III
0°	Contact force chain	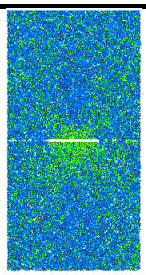	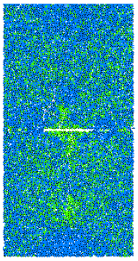	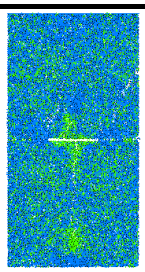
	Fracture classific ation			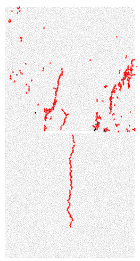
15°	Contact force chain	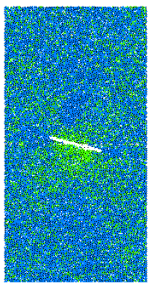	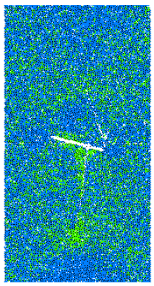	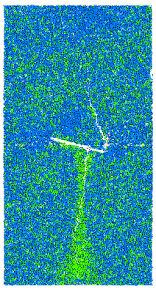
	Fracture classific ation	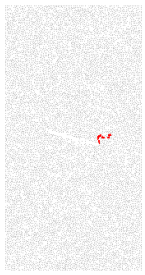	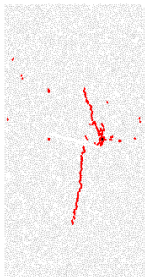	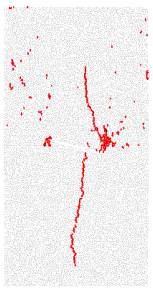
30°	Contact force chain	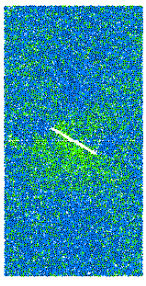	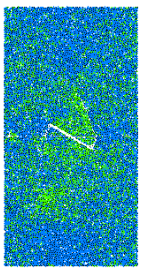	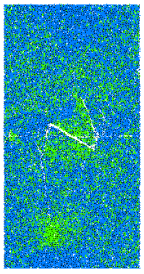
	Fracture classific ation		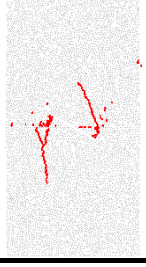	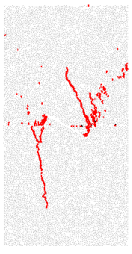

ISSN: 2710-0588

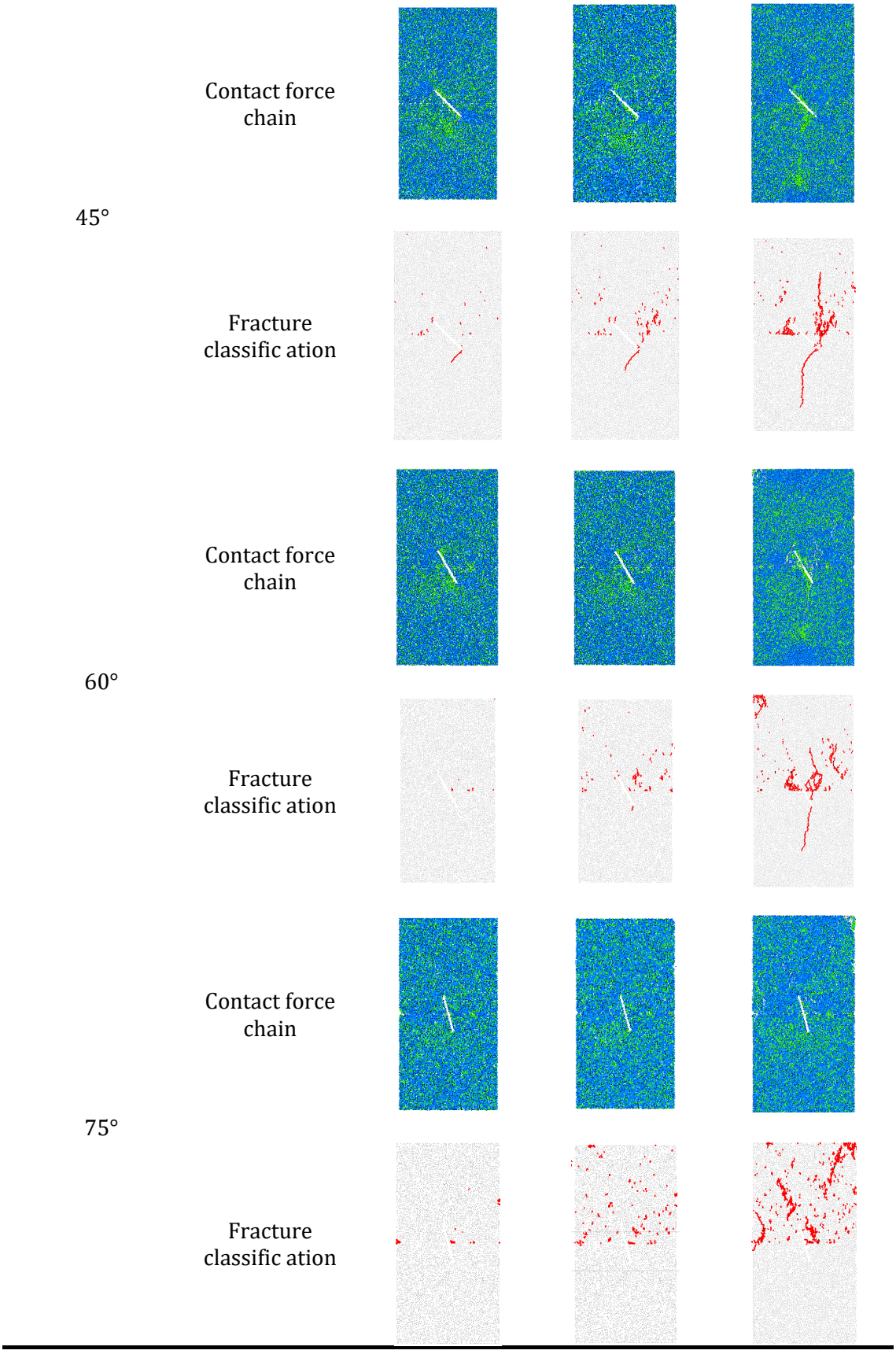

In the initiation location (I), the blue compressive force chains inside the specimen mainly extend along the loading direction, while the green tensile force chains mainly extend along the

ISSN: 2710-0588

horizontal direction. For the samples with crack dip angles of 0°-45°, obvious green tensile stress concentration is observed around and at the tips of the cracks; for the samples with crack dip angles of 60° and 75°, green tensile stress concentration and blue compressive stress concentration appear around the cracks. At this time, some maximum contact forces begin to exceed the strength of the force bonds, leading to their fracture. For the samples with fracture dip angles of 60° and 75°, microcracks first appear around the prefabricated cracks; for the samples with fracture dip angles of 0°, 15°, 30° and 45°, microcracks first appear at the tips of the prefabricated cracks, generally extending along the loading direction.

In the stable crack propagation stage (II), the distribution of contact force bonds inside the sample changes gradually. The stress at the tips of the prefabricated fractures of the samples with 0°-45° begins to distribute along the loading direction, and the concentrated stress of the samples with 60°-75° is still distributed at both ends and between the cracks. The samples with 0°-45° start to expand and extend continuously from the crack tips along the loading direction, and the samples with 60°-75° undergo uneven expansion in the upper half area of the sample, and the influence of prefabricated fractures begins to decrease gradually.

At the peak stress (III), an obvious zoning phenomenon appears in the particle contact network inside the sample. Stress concentration occurs at the tips of the samples with prefabricated fractures of 0°-45°, and microcracks expand along the loading direction and penetrate rapidly, forming a macroscopic fracture zone. However, no stress concentration is found at the tips of the samples with 60°-75°, among which the microcrack expansion of the 75° sample only occurs in the sandstone part. Red tensile cracks and black shear cracks are interwoven, among which red tensile cracks account for a relatively large proportion.

4.3. Final failure mode

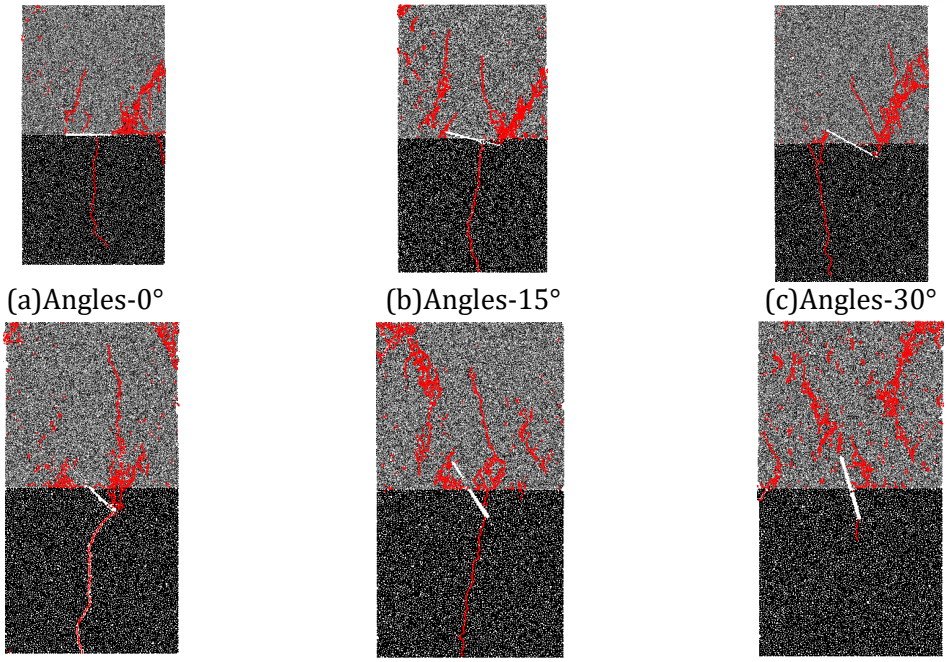

Figure 9. Final mode of destruction

The final failure modes of each sample under uniaxial compression are shown in the figure. When the dip angle of the prefabricated fracture is 0°, the cracks extend strictly vertically upward and downward from both ends of the horizontal fracture, forming two symmetrical, approximately parallel tensile wing cracks, followed by the appearance of secondary cracks and

ISSN: 2710-0588

scattered microcracks. The secondary cracks on the upper right side of the mixed rock mass sample expand steadily, and the tensile wing secondary cracks on the lower side of the mixed rock mass expand steadily without generating secondary cracks, with the failure being axial splitting.

When the dip angle of the prefabricated fracture is 15°, tensile wing cracks appear at the ends and middle of the prefabricated fracture, and the cracks still initiate from both ends of the fracture, but the propagation path is no longer vertical. The initiated wing cracks show a slight inclined expansion trend at a certain angle with the fracture surface and begin to try to align with the loading direction. The failure starts to transition from pure tension to tension-shear composite, but tension still dominates.

When the dip angle of the prefabricated fracture is 30°, in addition to the wing cracks initiated from the upper end of the fracture and expanding outward, reverse extending secondary inclined cracks appear at the lower end of the fracture. These cracks tend to expand to the other end of the prefabricated fracture and eventually often lead to an inclined main fracture zone penetrating the sample. At this time, shear sliding and tensile initiation jointly dominate the failure process.

When the prefabricated dip angle is 45°, the new cracks mainly extend and penetrate along the strike of the prefabricated fracture itself, forming clear shear cracks. The cracks are generated and connected almost close to both ends of the prefabricated fracture, indicating that obvious shear sliding occurs in the prefabricated fracture and directly controls the final failure surface, resulting in shear failure.

When the fracture dip angle is 60°, due to the large fracture dip angle and high normal pressure, the failure is completed by multiple branch cracks. After the crack initiates from one end of the fracture, it deflects and bifurcates during the propagation process, and finally connects into a relatively rough macroscopic fracture zone. This is a compression-shear composite failure accompanied by local tensile bifurcation.

When the prefabricated fracture dip angle is 75°, the control effect of the prefabricated fracture itself on the fracture path is weakened. New cracks are far away from the fracture ends and generate nearly vertical tensile wing cracks in other stress concentration areas of the sample, and very steep short cracks almost parallel to the loading direction are initiated from the fracture ends. The final failure mode is closer to the vertical splitting of the sample without prefabricated fractures, but the overall strength is reduced due to the existence of fractures. The prefabricated fractures mainly play a role in strength weakening rather than path control.

5. Influence of Fracture Angle on Rock Energy Evolution

The rock deforms under the action of external load, and a part of the energy input from the outside is converted into elastic strain energy stored inside the rock mass, and the other part is dissipated due to internal damage evolution. When the elastic strain energy accumulated by the rock mass reaches its capacity limit, the rock mass will fail, accompanied by a sharp release of dissipated energy. According to the results shown in Figure 11, the following analysis can be drawn:

(1) In the linear elastic deformation stage, the change curves of the total input energy U and the elastic strain energy Ue basically overlap, indicating that the work done by the outside on the rock is almost completely converted into storable elastic strain energy. The internal damage of the rock is extremely slight in this stage, so the energy dissipation part is very limited.

(2) After entering the yield stage, the elastic strain energy storage still dominates the total energy, but the dissipated energy begins to show the first significant increase. This is mainly due to the inhomogeneity of the rock material, which leads to the gradual generation of

ISSN: 2710-0588

microcracks in local stress concentration areas, thus causing a part of the energy to be released in the form of dissipation.

(3) In the post-peak stage, the rock continues to absorb energy, but the elastic strain energy drops rapidly, and the corresponding dissipated energy rises sharply. This process reflects that the accumulated elastic strain energy is rapidly converted into dissipated energy, driving the further expansion of internal damage of the rock and eventually forming macroscopic failure.

It can be seen from Figure 10 that the change of fracture dip angle has a significant impact on the starting point of rock dissipated energy generation. In the dip angle range of 0° to 30°, with the increase of dip angle, the strain value at which dissipated energy begins to appear decreases gradually, indicating that the rock enters the damage evolution stage earlier when bearing the load, which reflects that its resistance to internal damage weakens with the increase of dip angle. On the contrary, when the fracture dip angle is in the range of 30° to 75°, with the continuous increase of dip angle, the strain value at which dissipated energy appears shows a gradually increasing trend, indicating that the rock can remain in an approximately elastic state for a longer time, delaying the occurrence of damage, i.e., its resistance to internal damage is enhanced with the increase of dip angle.

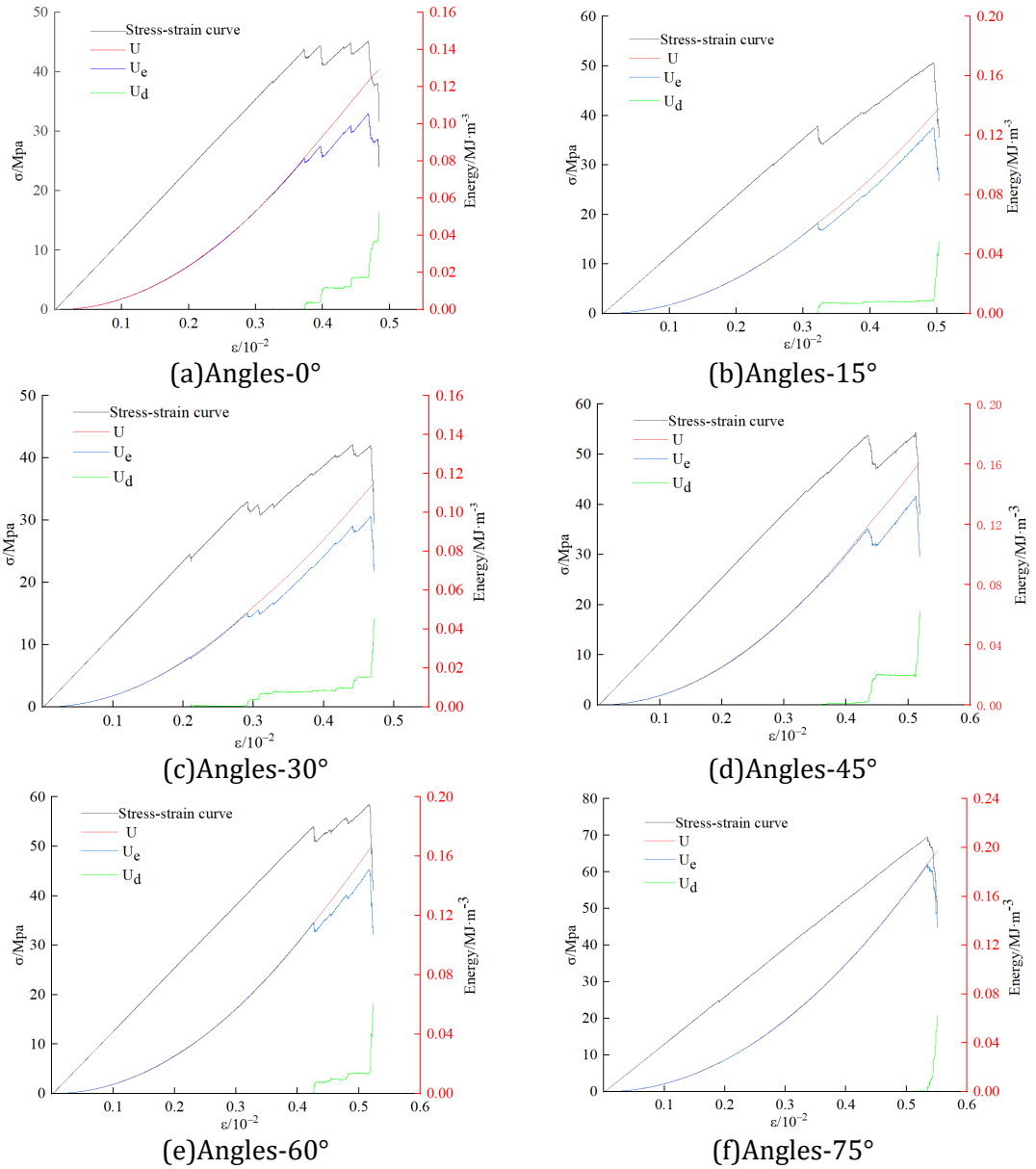

Figure 10. Energy conversion diagram of uniaxial compression test

ISSN: 2710-0588

6. Conclusion

(1) The fractured rock mass shows linear elastic deformation in the initial stage of loading, which conforms to Hooke's law. Among them, the rock mass with a fracture dip angle of 75° has the fastest stress growth, and that with 30° has the gentlest stress growth. When the strain exceeds the threshold, it enters the yield failure stage, and the peak stress and peak strain change regularly with the fracture dip angle: rising first and then falling in the range of 0°-30°, both reaching the minimum at 30°, and the fracture with this dip angle has the most significant degradation effect on the rock mass strength; rising continuously in the range of 30°-75° with an accelerated growth rate, both reaching the maximum at 75°, the fracture has the weakest degradation effect and its influence on the peak parameters far exceeds that of other dip angles.

(2) The influence of fracture length on the peak stress, peak strain and elastic modulus of rock mass is regulated by the fracture dip angle: at a fracture dip angle of 30°, the peak stress and peak strain decrease with the fracture length from 10 mm to 20 mm and rebound slightly at 25 mm, and the elastic modulus decreases with the increase of fracture length; at a dip angle of 60°, the peak stress and peak strain increase with the fracture length from 10 mm to 15 mm and decrease from 15 mm to 25 mm, the peak strain has a small fluctuation in the range of 15 mm to 25 mm, and the elastic modulus has no significant fluctuation. When the fracture dip angle is small (such as 30°), the fracture length has a significant impact on the mechanical parameters of the rock mass; when the dip angle increases to a specific value (such as 60°), its effect on the elastic modulus weakens, and the peak parameters show an opposite change law.

(3) With the increase of dip angle from 0° to 45°, the fracture zone turns from vertical to inclined, and its correlation with the prefabricated fracture changes from weak to strong with the strongest at 45°; after exceeding 45°, the fracture zone becomes complex or tends to be vertical again, and its geometric correlation with the prefabricated fracture weakens. 45° is the "optimal angle" for crack shear penetration along the prefabricated fracture surface.

(4) The dip angle range of 0°-30°, as the dip angle increases, the rock enters the damage evolution stage earlier, and its damage resistance decreases. In the 30°-75° range, with increasing dip angle, the onset of damage is delayed, and damage resistance is enhanced. Moreover, the total energy and elastic strain energy in each stage generally increase with increasing fracture dip angle, with a slight rebound in energy observed at dip angles of 15°-30°.

References

[1] Ohnaka, M., & Mogi, K. (1982). Frequency characteristics of acoustic emission in rocks under uniaxial compression and its relation to the fracturing process to failure. *Journal of Geophysical Research: Solid Earth*, 87(B5). https://doi.org/10.1029/JB087iB05p03873.

[2] Li, X. H., Niu, Z. J., Yao, Q. L., et al. (2020). Particle flow analysis of crack propagation characteristics of tripartite sandstone with cavity. *Journal of China Coal Society*, 45(11), 3735–3747.

[3] Yu, Q. J., Du, S. G., Zhang, Z. P., et al. (2025). Study on laboratory size effect of granite uniaxial compression considering crack propagation mechanism. *Rock Mechanics and Rock Engineering*, 1–20. [2025-11-21]. (Online advance publication)

[4] Wang, L. F., Tang, N., Yang, Z. Z., et al. (2025). Experimental study on the macro- and microscopic mechanical properties of fissured limestone under uniaxial compression. *China Rural Water and Hydropower*, 1–14. [2025-11-21]. (Online advance publication)

[5] Yi, T., Tang, J. X., & Wang, Y. L. (2021). Influence of fracture dip angle and number on rock mass strength and failure modes. *Journal of Underground Space and Engineering*, 17(1), 98–106, 134.

[6] Liu, W., Liu, Y. S., & Zhai, M. L. (2025). Study on energy dissipation and acoustic emission characteristics of red sandstone with intersecting fractures. *Journal of East China Jiaotong University*, 1–11. [2025-11-21]. (Online advance publication)

ISSN: 2710-0588

[7] Wang, X. R., Wang, E. Y., Liu, X. F., et al. (2018). Study on acoustic emission response and rate effect of crack propagation in fissured sandstone. *Chinese Journal of Rock Mechanics and Engineering*, 37(6), 1446–1458.

[8] Wang, X. R., Li, N., Wang, E. Y., et al. (2020). Quantitative inversion of acoustic emission for the microscopic mechanism of rock crack propagation. *Acta Geophysica Sinica*, 63 (7), 2627–2643.

[9] Fakhimi, A., Carvalho, F., & Ishida, T. (2002). Simulation of failure around a circular opening in rock. *International Journal of Rock Mechanics and Mining Sciences*, 39(4), 507–515. https://doi.org/10.1016/S1365-1609(02)00024-9

[10] Yin, P. F., & Yang, S. Q. (2019). Discrete element modeling of strength and failure behavior of transversely isotropic rock under uniaxial compression. *Journal of the Geological Society of India*, 93(2), 235–246. https://doi.org/10.1007/s12594-019-1173-9

[11] Huang, Y. H., Yang, S. Q., & Tian, W. L. (2019). Crack coalescence behavior of sandstone specimen containing two pre-existing flaws under different confining pressures. *Theoretical and Applied Fracture Mechanics*, 99, 118–130. https://doi.org/10.1016/j.tafmec.2018.12.006

[12] Cho, N., Martin, C. D., & Sego, D. C. (2007). A clumped particle model for rock. *International Journal of Rock Mechanics and Mining Sciences*, 44(7). https://doi.org/10.1016/j.ijrmms.2007.02.001

[13] Wang, Y. F., Song, M. Y., Jiao, H. Z., et al. (2024). Experimental study on the strength of granite under loading and unloading and its tendency for rockburst. *Journal of Mining and Rock Control Engineering*, 6(3), 47–56.

[14] Wang, Y. F., Yang, W. X., Jiao, H. Z., et al. (2016). Study on acoustic emission and damage characteristics simulation of brittle-ductile failure process of granite. *Journal of the Yangtze River Academy of Sciences*, 33(7), 76–80, 86.

[15] Liu, W. T., Zhou, Z. X., Su, M. M., et al. (2025). Experimental study on mechanical properties of marginally fractured red sandstone and crack propagation patterns. *Journal of Liaoning University of Engineering and Technology (Natural Science Edition)*, 1–10. [2025-12-07]. (Online advance publication)

[16] Liu, T. Y., Fan, J. S., & Peng, L. L. (2025). Analysis of rock strength and crack propagation with different fracture inclinations. *Journal of Railway Engineering*, 42(1), 1–6, 19.

[17] Zhou, X., Xiao, T. L., Hu, L., et al. (2025). Mechanical properties and crack propagation patterns of rock samples containing single-fracture layered composites. *Mining Research and Development*, 1–9. [2025-12-07]. (Online advance publication)

[18] Fan, X., Xie, Y. L., Lai, H. P., et al. (2018). Particle flow simulation of compression failure behavior of rock samples containing two joints. *Journal of Underground Space and Engineering*, 14(2), 461–469.

[19] Kang, Z. Q., Wang, Z. L., Feng, J. J., et al. (2024). Analysis of crack propagation in fractured sandstone after corrosion based on granular flow. *Metal Mines*, (2), 144–151.

[20] Zhu, D., Jing, H. W., Yin, Q., et al. (2019). Experimental study on mechanical characteristics of sandstone with arc-shaped prefabricated fractures. *Journal of China Coal Society*, 44(9), 2721–2732.

[21] Xia, M., & Zhao, C. B. (2014). Dimensional study on the influence of microscopic parameters on macroscopic parameters in the cluster parallel bond model. *Rock and Soil Mechanics*, 33(2), 327–338.

[22] Liu, X. R., & Yang, S. Q. (2018). Numerical study on micromechanical parameters of rocks based on orthogonal tests. *Journal of Applied Fundamentals and Engineering Sciences*, 26(4), 918–928.

[23] Cong, Y., Wang, Z. Q., Zheng, Y. R., et al. (2015). Experimental study on mesoscopic parameters of rock-like materials based on the principle of granular flow. *Journal of Geotechnical Engineering*, 37(6), 1031–1040.

[24] Chen, P. Y., Kong, Y., & Yu, H. M. (2018). Study on mesoscopic parameter calibration of rock uniaxial compression PFC2D model. *Journal of Underground Space and Engineering*, 14(5), 1240–1249.